Since January 2020 Elsevier has created a COVID-19 resource centre with free information in English and Mandarin on the novel coronavirus COVID-19. The COVID-19 resource centre is hosted on Elsevier Connect, the company's public news and information website.

Biomaterials 288 (2022) 121694

Contents lists available at ScienceDirect

Biomaterials

journal homepage: www.elsevier.com/locate/biomaterials

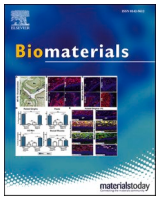

Ultrabright nanoparticle-labeled lateral flow immunoassay for detection of anti-SARS-CoV-2 neutralizing antibodies in human serum

Lun Bian [a,1], Zhaoyue Li [b,1], An He [c,1], Biru Wu [a], Hui Yang [a], Yingsong Wu [b,***], Fang Hu [a,*], Guanfeng Lin [d,**], Deqing Zhang [e]

[a] Guangdong Province Key Laboratory of Construction and Detection in Tissue Engineering, Biomaterials Research Center, School of Biomedical Engineering, Southern Medical University, Guangzhou, China
[b] Key Laboratory of Antibody Engineering of Guangdong Higher Education Institutes, Institute of Antibody Engineering, School of Laboratory Medicine and Biotechnology, Southern Medical University, Guangzhou, China
[c] The First People's Hospital of Chenzhou City, Chenzhou, China
[d] Experimental Center of Teaching and Scientific Research, School of Laboratory Medicine and Biotechnology, Southern Medical University, Guangzhou, China
[e] Beijing National Laboratory for Molecular Sciences, CAS Key Laboratory of Organic Solids, Institute of Chemistry, Chinese Academy of Sciences, Beijing, China

ARTICLE INFO

Keywords:
Aggregation-induced emission
SARS-CoV-2
Neutralizing antibody
Lateral flow immunoassay

ABSTRACT

The level of anti-SARS-CoV-2 neutralizing antibodies (NAb) is an indispensable reference for evaluating the acquired protective immunity against SARS-CoV-2. Here, we established an ultrabright nanoparticles-based lateral flow immunoassay (LFIA) for one-step rapid semi-quantitative detection of anti-SARS-CoV-2 NAb in vaccinee's serum. Once embedded in polystyrene (PS) nanoparticles, the aggregation-induced emission (AIE) luminogen, AIE_{490}, exhibited ultrabright fluorescence due to the rigidity of PS and severe inhibition of intramolecular motions. The ultrabright AIE_{490}-PS nanoparticle was used as a fluorescent marker of LFIA. Upon optimized conditions including incubation time, concentrations of coated proteins and conjugated nanoparticles, amounts of antigens modified on the surface of nanoparticles, dilution rate of serum samples, and so on, the ultrabright nanoparticles-based LFIA could accurately identify 70 negative samples and 63 positive samples from human serum ($p < 0.0001$). The intra- and inter-assay precisions of the established method are above 13% and 16%, respectively. The established LFIA has tremendous practical value of generalization as a rapid semi-quantitative detection method of anti-SARS-CoV-2 NAb. Meanwhile, the AIE_{490}-PS nanoparticle is also promising to detect many other analytes by altering the protein on the surface.

1. Introduction

The coronavirus disease 2019 (COVID-19) caused by novel severe acute respiratory syndrome coronavirus 2 (SARS-CoV-2) has become a global pandemic [1]. By the end of 2021, over 300 million people worldwide had been infected with SARS-CoV-2 and over 5 million people have died. At present, vaccination against SARS-CoV-2 is the key strategy to prevent this infectious disease [2]. Valid methods to evaluate the acquired immunity after vaccination are highly demanded. Testing of specific immunoglobulin M (IgM) and immunoglobulin G (IgG) against SARS-CoV-2 is commonly used to evaluate the effect of the vaccine [3]. However, only a small portion of the IgM and IgG can neutralize and resist SARS-CoV-2 [4], the positive detection of the specific IgM and IgG is not a reliable evaluation of acquired immunity against SARS-CoV-2. The viral entry of SARS-CoV-2 is mediated through the recognization of angiotensin-converting enzyme 2 (ACE2) on the human cell surface by the receptor-binding domain (RBD) in the spike protein of SARS-CoV-2 [5]. The acquired neutralizing antibodies (NAbs) after vaccination can competitively bind the RBD and neutralize SARS-CoV-2 [4]. Therefore, the direct detection of NAbs is a more accurate method to evaluate the effect of the vaccine [6,7]. Meanwhile, the detection of NAbs in human body could synergistically guide the vaccine

* Corresponding author.
** Corresponding author.
*** Corresponding author.
E-mail addresses: wg@smu.edu.cn (Y. Wu), hufang19@smu.edu.cn (F. Hu), lingf@smu.edu.cn (G. Lin).
[1] These authors contributed equally to this work.

https://doi.org/10.1016/j.biomaterials.2022.121694
Received 21 March 2022; Received in revised form 13 July 2022; Accepted 20 July 2022
Available online 9 August 2022

strategies against new viral variants with particular reference [8].

The conventional virus neutralization tests require biosafety level 3 facilities due to the live virus operations, and the pseudovirus-based virus neutralization tests require biosafety level 2 facilities. The high-standard conditions cost much and require professional operator, which is unpractical for massive detection of NAbs. Therefore, several convenient methods, such as lateral flow immunoassay (LFIA) [9], enzyme-linked immunosorbent assay [10], surface plasmon resonance assay [11], and some emerging digital microfluidic systems [12–14], have been developed to detect SARS-CoV-2 NAbs recently. Among all of them, the LFIA method enjoys portability, rapidity, simplicity, and low cost, and it has been widely used in the point-of-care immunosensors. For example, the colloidal gold nanoparticles- [15] and colored cellulose nanobeads-based LFIA [16] were developed to detect the SARS-CoV-2 NAbs very recently. However, the sensitivity is insufficient and the linear range is usually narrow due to their restricted colorimetric signal. Fortunately, the fluorescent signal can provide higher sensitivity and the fluorescent marker-based LFIAs can improve the work linear range. Generally, the immunoassays contain competitive immunoassay and sandwich immunoassay. The sandwich immunoassay commonly has higher sensitivity and specificity. However, the NAb is a series of antibodies that can neutralize SARS-CoV-2, whose components are complex. It is hard to find two different binding sites on NAb. Therefore, the sandwich immunoassay is not suitable for NAb detection. Meanwhile, the direct competitive immunoassay is cheaper and more reliable than the sandwich immunoassay, the batch-to-batch variation is smaller, which is important for massive detection of NAbs. The direct competitive immunoassay was used in this study.

The sensitivity of the fluorescent marker-based LFIA highly depends on the working fluorescent materials [17]. Bright nanomaterials such as quantum dots (QDs) [18] and lanthanide-based microspheres [19] are commonly used in LFIAs. Compared to the metallic luminophores, the color and fluorescence wavelength of organic luminogens can be easily tuned through engineering of chemical structures [20]. However, most luminogens undergo aggregation-caused quenching (ACQ) due to strong π−π stacking in aggregate state when they are introduced into nanoparticles or self-aggregation at the test line, which would reduce the detection performance of LFIA [21]. Recently, organic luminogens with aggregation-induced emission (AIEgens) have drawn broad attention because of their bright fluorescence in aggregate state or at high concentrations, which can overcome the drawback of traditional luminogens [22]. Since the bright fluorescence of AIEgens comes from the intramolecular rotation restriction and inhibition of nonradiative decay, the denser the packing of AIEgens, the brighter the fluorescence is [23]. Therefore, the AIEgens are generally used in dense packing formats such as surfactant matrix-AIEgen nanoparticles [24], amorphous or crystalline precipitates [25]. The surfactant matrix-AIEgen nanoparticles and amorphous precipitates can restrict intramolecular rotation and shield the influence of water, enabling bright fluorescence of the AIEgens [23]. But their packing is much looser than in crystalline state, in which the AIEgen molecules are orderly and densely packed with less intramolecular rotation and ultrabright fluorescence [25]. However, the nanocrystal of AIEgen is suffered from difficult conjugation with antibodies and difficult release from the pad, which restricts the utilization of the ultrabright AIEgen nanocrystal in LIFA. To introduce the ultrabright AIEgens into LIFA, the proper format of the AIEgens is desired.

In this work, we established an AIEgen-embedded polystyrene (PS) nanoparticles-based LFIA, and successfully detected the anti-SARS-CoV-

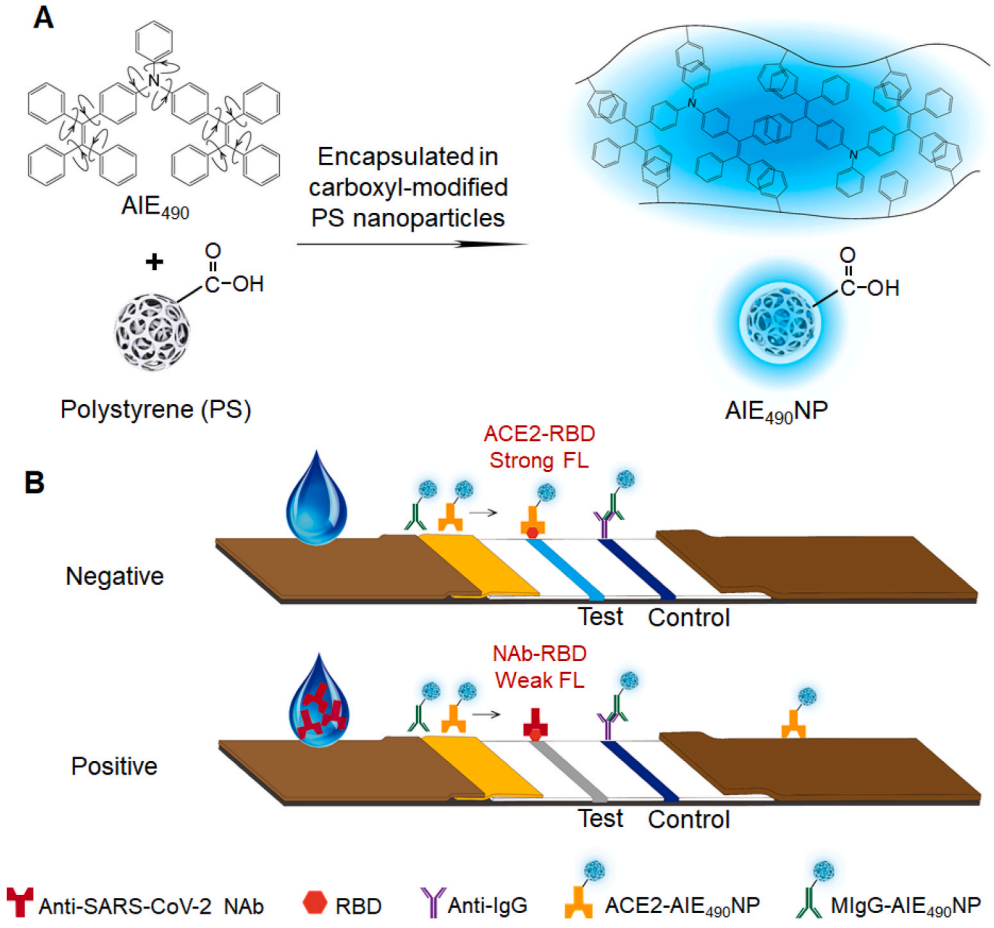

Scheme 1. (A) Preparation of $AIE_{490}NP$. (B) Schematic of the developed $AIE_{490}NP$-based LFIA test strip for detection of anti-SARS-CoV-2 NAbs in human serum sample.

2 NAb in serum from the vaccinees. PS is a rigid polymer with hydrophobic chains and steric phenyl rings. We hypothesized that the rigidity of PS particles could severely inhibit the intramolecular motions and trigger ultrabright fluorescence once the AIEgen is embedded into PS particles. Our study showed that the fluorescence signal of a green blue-emissive AIEgen (AIE_{490}) was enhanced more than 10 times after being encapsulated into the carboxyl-modified PS nanoparticles ($AIE_{490}NP$), which was also much brighter than QDs (Scheme 1A). The $AIE_{490}NP$ was modified with ACE2 Fc chimera (ACE2-$AIE_{490}NP$) as a fluorescence marker; the SARS-CoV-2 nucleocapsid S RBD fusion was coated on the nitrocellulose membrane as a test line. When the sample was negative (without NAbs), the test line exhibited bright fluorescence signal due to the strong ACE2-RBD binding; when the sample was positive (with NAbs), the test line exhibited a dim fluorescence signal due to the inhibition of ACE2-RBD binding through NAb-RBD binding (Scheme 1B). Benefiting from the ultrabright fluorescence of $AIE_{490}NP$, 63 positive serum samples from vaccinees and 70 pre-SARS-CoV-2 serum samples were accurately identified by using the $AIE_{490}NP$-based LFIA. Theoretically, the concentrations of NAbs could also be quantified by using the $AIE_{490}NP$-based LFIA if the standard sample of NAbs is available. Meanwhile, one detection could be finished within 20 min, and the LFIA strip is portable and costless, which is important for widespread applications of SARS-CoV-2-related antibody detection and vaccination study.

2. Experimental section

2.1. Synthesis of $AIE_{490}NP$

The $AIE_{490}NP$ was assembled by encapsulating AIE_{490} into the 200 nm carboxyl-modified PS nanoparticles through the swelling method. First, 10 mg of PS nanoparticles were resuspended thoroughly in 1 mL of 2.5% SDS solution using a UP200S probe ultrasonic crusher (Hielscher, Teltow, Germany), and then 100 μg of AIE_{490} dissolved in 100 μL of THF was added. The mixture was then stirred for 4 h at room temperature. After centrifugation at 25,000*g* for 30 min and removing the supernatant, the $AIE_{490}NP$ were resuspended in 1 mL of ultrapure water and stored at 4 °C for future use.

2.2. Characterization of AIE_{490} and $AIE_{490}NP$

The Nuclear Magnetic Resonance Spectra (NMR) of AIE_{490} were collected using an AscendTM400 spectrometer (Bruker Daltonics Inc., Germany). The UV–vis absorption and emission were obtained using a UV–vis spectrophotometer (Shimadzu, Japan) and a Lumina spectrophotometer (Thermo Fisher Scientific Inc., USA), respectively. The hydrodynamic diameter and zeta-potential were characterized using a Nano-ZS90 ZetaSizer (Malvern Panalytical Ltd., UK). The transmission electron microscopy (TEM) images were taken with an H-7500 transmission electron microscope (Hitachi Co., Ltd., Japan). The photoluminesce quantum yields (PLQYs) of AIE_{490} molecules aggregated in water, AIE_{490}-DSPE-PEG, $AIE_{490}NP$, QD-NP-525, and QD-NP-545 were measured using quinine sulphate (QY = 58%) in water as a reference.

2.3. Preparation of $AIE_{490}NP$ conjugated with ACE2 and MIgG

The $AIE_{490}NP$-ACE2 conjugation and $AIE_{490}NP$-MIgG conjugation were prepared by the EDC-NHS method. Initially, 1 mg of $AIE_{490}NP$ was centrifuged to remove the storage solution and then resuspended in 500 μL of activating buffer containing 0.625 μmol of EDC and 5 μmol of sulfo-NHS. The interactant was gently shaken for 30 min at room temperature for activation, and then centrifuged to separate the activated $AIE_{490}NP$. The activated $AIE_{490}NP$ was then washed two times using washing buffer and resuspended in 300 μL of binding buffer. Then, the activated $AIE_{490}NP$ was added with 50 μg of ACE2 protein which was purified and condensed into 200 μL of the binding buffer using a centrifugal filter unit with an Ultracel-10 membrane and stirred for 2 h to form a bipartite complex of $AIE_{490}NP$-ACE2. The complex was then mixed with 500 μL of blocking buffer containing 5% BSA and incubated at room temperature for another 2 h to block the unreacted NHS ester on the surface of activated $AIE_{490}NP$. After incubation, the $AIE_{490}NP$-ACE2 was centrifuged to remove the unreacted reagent, unconnected ACE2 antigen, and binding buffer, and then redispersed in labeling antibody storage buffer and stored at 4 °C for further use. The conjugation procedure of $AIE_{490}NP$-MIgG was similar to that of $AIE_{490}NP$-ACE2, except the ACE2 protein was replaced with MIgG.

2.4. Treatment of sample pad, conjugate pad, and absorbent pad

The glass fiber was cut into 300 × 21 mm and 300 × 12 mm pieces to obtain untreated sample pads and conjugate pads. The pads were then soaked in the equivalent treatment buffer for 2 h at room temperature and dried at 37 °C for 24 h in a cabinet drier to gain sample pad and conjugate pad. The absorbent pad was 300 × 26 mm pieces cut from whole one without other treatment. All those pads were stored in a moisture-proof cabinet.

2.5. Preparation of $AIE_{490}NP$-based LFIA test strip

The $AIE_{490}NP$-based LFIA test strip is composed of five ingredients: sample pad, conjugate pad, absorbent pad, nitrocellulose membrane, and plastic adhesive backing plate. The RBD recombinant protein and anti-IgG were prediluted using coating buffer and then sprayed equably on the nitrocellulose membrane as test line and control line respectively. The nitrocellulose membrane was then stuck on the backing plate and dried overnight at 37 °C. The $AIE_{490}NP$-ACE2 and $AIE_{490}NP$-MIgG prediluted in labeling antibody dilution buffer were both spotted onto pretreated conjugate pad with a ratio of 10 μL/cm following by dried overnight at 37 °C. The five components were assembled sequentially to ensure a direct flow from sample pad to absorbent pad under capillarity. Last, the well-assembled plate was cut into 4 mm wide strips using a strip cutter. Each strip was packaged into a strip shell with a circular sample loading hole and a rectangular viewing window for further use.

3. Results

3.1. Synthesis and characterization of $AIE_{490}NP$

AIE_{490} is a green blue-emissive AIEgen with a fluorescence peak at 490 nm. It is constructed by typical AIE units including tetraphenylethylene and triphenylamine. The synthetic pathway of AIE_{490} is detailedly described in the supporting information (Scheme S1), and the chemical structure and purification were characterized by NMR (Fig. S1) and mass spectrometry (Fig. S2). The simple synthetic procedure with high yield is advantageous for large-scale production. The absorbance and fluorescence spectra of AIE_{490} molecules aggregated in water (THF/water, v/v = 1/99, 10 μg/mL) were shown in Fig. S3. The absorbance maximum is 362 nm and the fluorescence maximum is 494 nm.

The AIE properties of AIE_{490} were examined by measuring the fluorescence intensity in THF/water mixtures with varied water fractions (f_w, vol%). With the increasement of the water fractions, the fluorescence intensity of AIE_{490} increased gradually from 0 to 80% and increased significantly from 80 to 99%, exhibiting typical AIE properties (Fig. 1A).

The stability of AIE_{490} was evaluated by monitoring the changes of fluorescence intensity under continuous irradiation of white light (100 mW/cm^2, measured by LWP10W-A optical power meter (Beijing Laserwave OptoElectronics Technology Co., Ltd)), or under different storage temperatures and pH. The AIE_{490} exhibited a loss of only 8.0% in fluorescence intensity after 60 min irradiation (Fig. S4), indicating excellent photostability. The fluorescence intensity of AIE_{490} at different temperatures (10–50 °C) exhibited at most 1.6% of loss (Fig. S5 and

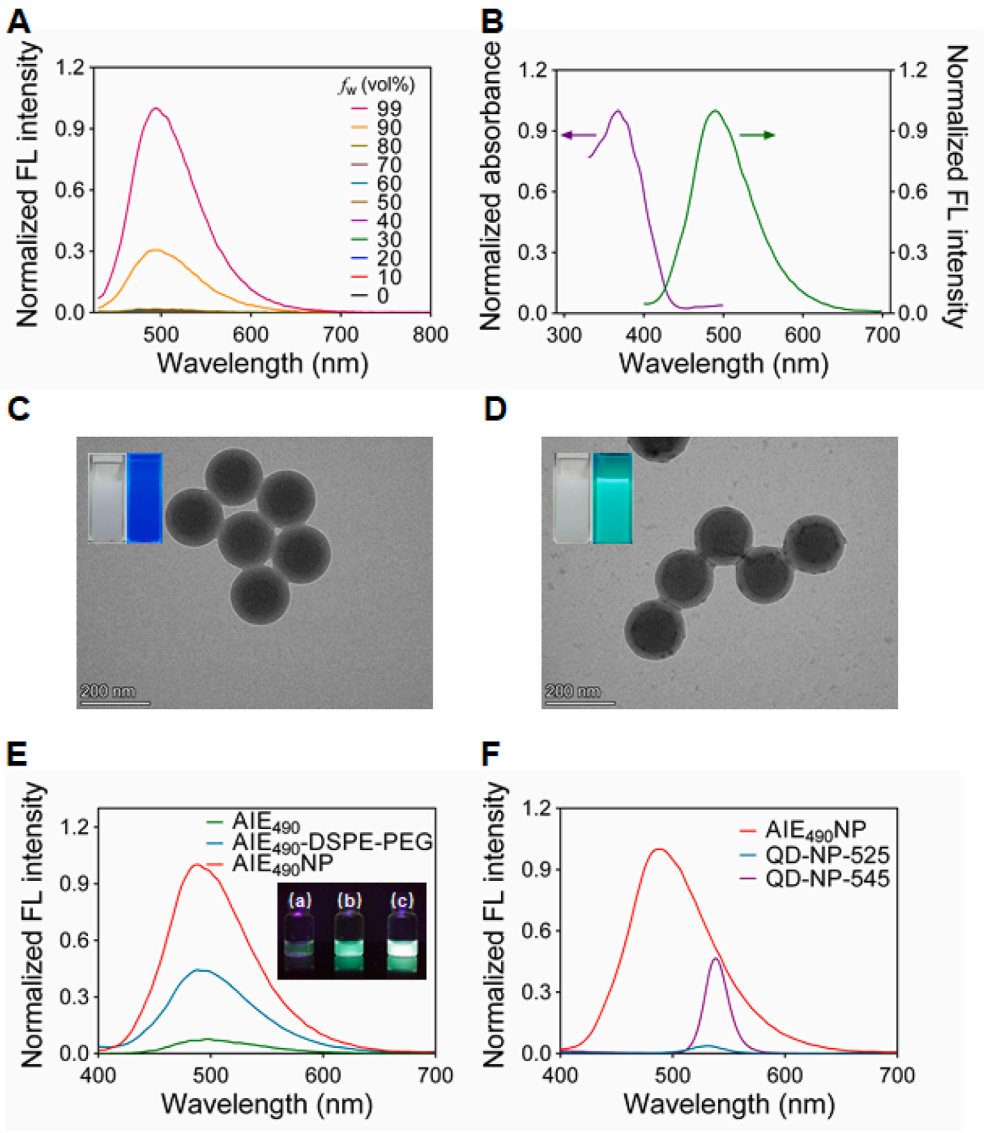

Fig. 1. (A) Fluorescence spectra of AIE_{490} in THF and THF/water mixture with different water fractions (f_w). (B) Absorption and fluorescence spectra of $AIE_{490}NP$, λ_{ex} = 365 nm. The TEM images of PS nanoparticles (C) and $AIE_{490}NP$ (D), the insets show the image of PS nanoparticles and $AIE_{490}NP$ under visible light and UV light, respectively. (E) The fluorescence intensity of AIE_{490} aggregated in water, AIE_{490}-DSPE-PEG, and $AIE_{490}NP$, the insets show the fluorescence under UV light, λ_{ex} = 365 nm (a is AIE_{490} aggregated in water, b is AIE_{490}-DSPE-PEG, and c is $AIE_{490}NP$). The amount of AIE_{490} aggregated in water was equal to that encapsulated in DSPE-PEG nanoparticles and PS nanoparticles to be 1 μg. (F) The fluorescence spectra of $AIE_{490}NP$ and two QPs, λ_{ex} = 365 nm. The concentrations of the three nanoparticles were all 0.1 mg/mL.

Table S1), while those stored at different pH (5.5–9.0) exhibited at most 5.6% of loss (Fig. S6 and Table S2), demonstrating excellent stability against different temperature and pH. The high stability of AIE_{490} is beneficial to reliable detection.

For diagnostic applications, the AIE_{490} molecules were then encapsulated into carboxyl-modified PS nanoparticles using organic solvent swelling method to gain $AIE_{490}NP$. AIE_{490} can dissolve well in THF at above 4 mg/mL. The well-solubility in THF allows AIE_{490} to be efficiently encapsulated into PS nanoparticles by swelling method. The optical properties of $AIE_{490}NP$ were characterized using UV–vis and fluorescence spectroscopy, the absorbance maximum and fluorescence maximum are similar to the aggregates in water. The maximum absorption and emission of $AIE_{490}NP$ were 365 nm and 490 nm, respectively (Fig. 1B). Fig. 1C and D showed the TEM images of PS nanoparticles and $AIE_{490}NP$, whose sizes and morphologies were almost the same. The hydrodynamic diameter and zeta potential of $AIE_{490}NP$ were measured to be 180 nm and −53.7 mV, which were also similar to the PS nanoparticles (Figs. S7–S8). The negative zeta potential came from the carboxyl groups on the surface. The insignificant differences in hydrodynamic diameters and zeta potential indicated that the encapsulation of AIE_{490} would not damage the PS nanoparticles. The insets of Fig. 1C and D are the pictures of PS nanoparticles and $AIE_{490}NP$ under visible light and UV light, respectively. The strong fluorescence of the obtained $AIE_{490}NP$ indicated successful encapsulation of AIE_{490} into PS nanoparticles. By fitting a response curve of absorption at 365 nm, the number of AIE_{490} molecules in an $AIE_{490}NP$ was estimated to be 3.4×10^4 (Fig. S9).

To confirm the performance of $AIE_{490}NP$, we observed the fluorescence intensity of $AIE_{490}NP$ and the equivalent AIE_{490} molecules aggregated in water or embed in DSPE-PEG nanoparticles (AIE_{490}-DSPE-PEG). The FL signal of $AIE_{490}NP$ was 14 times as strong as the aggregate in water, 2 times as strong as AIE_{490}-DSPE-PEG (Fig. 1E). The PLQYs of AIE_{490} aggregated in water, AIE_{490}-DSPE-PEG and $AIE_{490}NP$ were measured as 31.4%, 26.9% and 33.6%, respectively. Since polystyrene also has an absorbance at the excitation wavelength, the PLQY of $AIE_{490}NP$ is only slightly higher than AIE_{490} molecules aggregated in water though $AIE_{490}NP$ is much brighter under the same photoexcitation. The ultrabright fluorescence of $AIE_{490}NP$ came from the shielding of water by the hydrophobic chains of PS and the severe inhibition of intramolecular motions by the rigidity of PS. Moreover, we compared the fluorescence intensity of $AIE_{490}NP$ with two QD-doped PS nanoparticles (QPs) that had been reported in our previous studies [26,27]. The $AIE_{490}NP$ also exhibited fluorescence intensity dozens of times that of QPs (Fig. 1F and Fig. S10). The PLQYs of QD-NP-525 and QD-NP-545 were 11.9% and 7.2%, respectively, which were much lower than the AIE_{490}-based groups. The $AIE_{490}NP$ has the similar stability properties to

AIE_{490} against continuous irradiation (Fig. S4), different temperatures (Fig. S5 and Table S1) and pH (Fig. S6 and Table S2). Meanwhile, the hydrodynamic diameters of AIE_{490}NP at different temperatures or pH were maintained at 172.8–196.4 nm or 172.8–196.4 nm (Fig. S11), respectively, indicating excellent structural stability of AIE_{490}NP against temperature and pH.

3.2. Preparation and characterization of AIE_{490}NP-antigen conjugation

The preparation of AIE_{490}NP-antigen conjugations was accomplished through activation of carboxyl on AIE_{490}NP and coupling with amine on the antigens (Fig. 2A). To ensure the successful conjugation of AIE_{490}NP with ACE2 or MIgG, the hydrodynamic diameter and zeta potential of AIE_{490}NP, AIE_{490}NP-ACE2, and AIE_{490}NP-MIgG were characterized. After modification of ACE2 and MIgG, the hydrodynamic diameters slightly increased from 180 nm to 230 nm and 250 nm, respectively (Fig. 2B). The zeta potentials also changed from −53.7 mV to −29.9 mV and −34.3 mV after the connection with the antigens (Fig. 2C). The increased zeta potentials were due to the block of negative carboxyl groups. Meanwhile, the ACE2 and MIgG could be directly observed in the TEM images of AIE_{490}NP-ACE2 (Fig. 2D) and AIE_{490}NP-MIgG (Fig. 2E), which further supported the successful conjugation. To further verify the protein modification, surface plasmon resonance (SPR) was used to detect the affinity of AIE_{490}NP-ACE2/RBD and AIE_{490}NP-MIgG/anti-IgG (Fig. S12). By linking RBD or anti-IgG to the surface of 3D Dextran chip as ligands, the dissociation equilibrium constants of AIE_{490}NP-ACE2/RBD and AIE_{490}NP-MIgG/anti-IgG were tested to be 101 pM and 87 pM (Table S3), respectively, indicating the successful modification of ACE2 and MIgG onto AIE_{490}NP. Meanwhile, the conjugation with antigens hardly influenced the fluorescence intensity of AIE_{490}NP (Fig. S13).

3.3. Working mechanism of the AIE_{490}NP-based LFIA

Based on the recognition interaction between ACE2 and RBD, and the binding interaction between NAb and RBD, the AIE_{490}NP-based LFIA was performed as a typical competitive immunoassay. The picture of the LFIA product was shown in Fig. 3A. The RBD was coated as the test line, the anti-IgG was coated as the control line. The sample buffer containing human anti-SARS-CoV-2 NAb was dropped to the sample pad following by migration to the conjugate pad, and gradually carried the AIE_{490}NP-ACE2 and AIE_{490}NP-MIgG immobilized on the conjugate pad towards absorbent pad by capillarity. Once the mixture reached the test line, the anti-SARS-CoV-2 NAb would bind the SARS-CoV-2 RBD to prevent it from recognizing human ACE2, which would lead to a weaker fluorescent signal of the test line (H_T). The higher the NAb concentration, the weaker the fluorescent signal would be. When the sample was negative, no competition happened to break the ACE2-RBD binding, and the AIE_{490}NP-ACE2 would stay on the test line, exhibiting strong fluorescent signals. Meanwhile, the binding between anti-IgG and MIgG was not influenced so that the fluorescent signal of the control line (H_C) was undisturbed by anti-SARS-CoV-2 NAb in the serum sample. Fig. 3B showed the pictures of the visual detection results upon 365 nm irradiation for several positive and negative samples. The test line of the

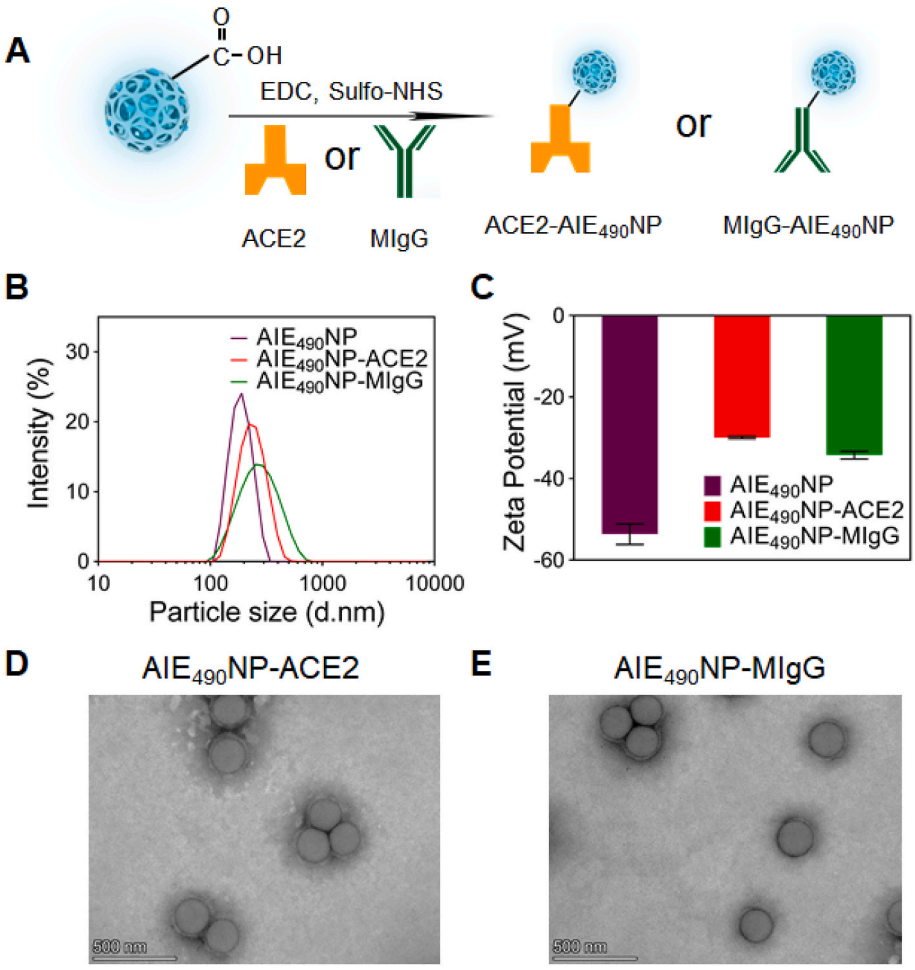

Fig. 2. (A) The conjugation process of AIE_{490}NP-ACE2 and AIE_{490}NP-MIgG. The hydrodynamic diameters (B) and zeta potentials (C) of AIE_{490}NP, AIE_{490}NP-ACE2, and AIE_{490}NP-MIgG. The TEM images of AIE_{490}NP-ACE2 (D) and AIE_{490}NP-MIgG (E).

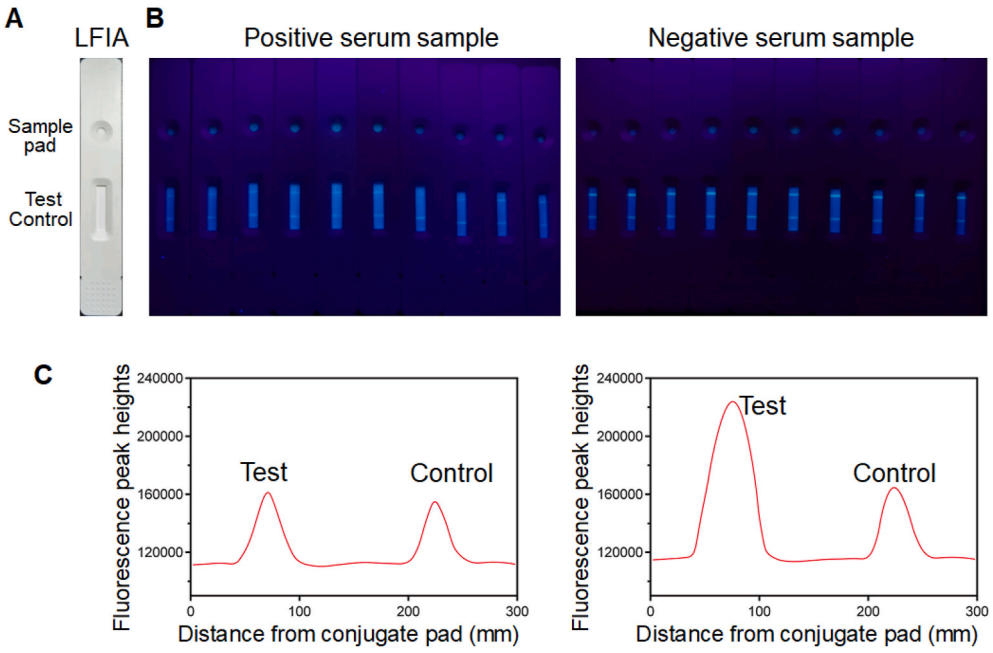

Fig. 3. (A) The picture of the AIE_{490}NP-based LFIA product. (B) The pictures of the visual detection results upon 365 nm irradiation for several positive and negative samples. (C) The fluorescence peak heights readout curve of positive and negative samples using.

negative samples was apparently brighter than that of the positive samples. After 20 min incubation, the test strip was measured using a portable fluorescence reader to obtain H_T and H_C (Fig. 3C).

To visually demonstrate the excellent performance of the ultrabright AIE_{490}NP in LFIA, the QD-NP-525 and QD-NP-545 were also conjugated with ACE2 and MIgG to serve as fluorescent markers in the LFIA. As shown in Fig. S14, the LFIA test strip with AIE_{490}NP exhibited a much higher fluorescence signal than QD-NP-525 and QD-NP-545 on the fluorescent band, indicating better potential in LFIA applications.

To counteract the intrinsic heterogeneity of the AIE_{490}NP-based LFIA and the influence of serum matrix, the ratio of H_T and H_C was used as the final result of a test strip, which would make the results more reliable and reproducible. The inhibition rate was calculated to further confirm the inhibitory effect of the NAb in the serum sample on the RBD binding ability by the following equation:

$$\text{Inhibition rate} = \frac{(R_0 - R)}{R_0} * 100\%$$

where R_0 is the H_T/H_C ratio of sample buffer, R is the H_T/H_C ratio of the sample. Meanwhile, the signal-to-noise ratio was evaluated through the ratio of the inhibition rates between positive and negative samples, to confirm whether the AIE_{490}NP-based LFIA could effectively distinguish the negative and positive serum samples.

3.4. Optimization of the antibody-antigen recognition conditions

The detection performance of an LFIA method also highly depends on the antibody-antigen recognition conditions, including recognition time, the concentration of protein coating on test/control line, the amount of protein modified on fluorescent nanoparticles, the usage amount of modified fluorescent nanoparticles, and so on. As shown in Fig. 4A, over the range of 10–40 min of incubation after loading to test strip, the H_T/H_C ratios of sample buffer and negative sample reached a plateau at 20 min while that of the positive sample stayed stable. The inhibition rates of the negative and positive samples both reached a plateau after 20 min of incubation (Fig. 4B). The signal-to-noise ratio reaches a plateau at 15 min and its coefficient of variation (CV%) stabilizes at a low level after 20 min incubation (Fig. S15). According to the changing trend of inhibition rate and signal-to-noise ratio, it can be found that the detection requirements can be met at 10 min. However, the instability of positive results at 10 min may lead to unreliable outputs. Furthermore, since the established LFIA is for qualitative or semi-

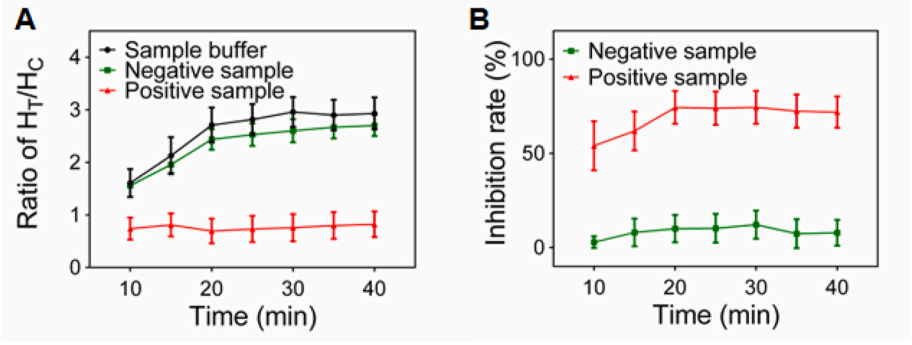

Fig. 4. (A) The H_T/H_C ratios of sample buffer, negative samples, and positive samples under different incubation time. The average and standard deviation were calculated through five replications. (B) The inhibition rates of negative samples, and positive samples under different incubation time. The average and standard deviation were calculated through five replications.

quantitative detection, consistency of results is more important. Therefore, we finally chose 20 min as the incubation time for the LFIA.

To figure out the optimized concentrations of RBD and anti-IgG coating onto nitrocellulose membrane, we selected 0.5, 1, and 2 mg/mL as alternatives. The results of the cross-pairing experiment showed that the H_T/H_C ratios of all sample buffer, negative sample, and positive sample heightened following the increase of RBD concentrations and decrease of anti-IgG concentrations (Fig. S16); the differences of inhibition rates between the negative and the positive samples reached a peak when the concentration of RBD is 1 mg/mL, and they are hardly related to the concentration of anti-IgG (Fig. S17). Comprehensively, the signal-to-noise ratios of all the samples were figured out by the values of the H_T/H_C ratios and the inhibition rates (Fig. 5). The signal-to-noise ratio reached the highest when the concentration of RBD was 1 mg/mL, the concentration of anti-IgG was 2 mg/mL, which were selected as the optimized coating concentrations.

We also assessed whether the amount of ACE2 modified on the surface of $AIE_{490}NP$ would affect the detection results. As the ACE2 modified on the surface of each milligram of $AIE_{490}NP$ increased from 25 μg to 100 μg, the H_T/H_C ratio of sample buffer, negative samples, and positive samples all increased (Fig. S18) while the inhibition rates of all negative and positive samples kept stable (Fig. S19). The signal-to-noise ratio reached the highest when the surface-modified protein was 50 μg (Fig. 6A).

Furthermore, we optimized the usage amount of the $AIE_{490}NP$-ACE2. The H_T/H_C ratio increased significantly with the increase of $AIE_{490}NP$-ACE2 antigen concentration from 62.5 to 1000 μg/mL (Fig. S20). At the same time, the inhibition rate of the positive sample reached the peak when the concentration of $AIE_{490}NP$-ACE2 antigen was 250 μg/mL, while that of the negative sample decreased along with the increasing concentration of $AIE_{490}NP$-ACE2 (Fig. S21). The signal-to-noise ratio reached the highest when the concentration of $AIE_{490}NP$-ACE2 was 250 μg/mL (Fig. 6B).

3.5. Optimization of the dilution ratio of clinical serum samples

To achieve the highest signal-to-noise ratio, the dilution ratio of clinical serum samples was optimized. Both negative serum samples and positive serum samples were prediluted using sample buffer with the ratio of 1/5, 1/10, 1/20, and 1/40 before loading onto the test strip. After 20 min of incubation, each test strip was loaded into a fluorescence reader to obtain the fluorescent intensities of the test line (H_T) and the control line (H_C). The H_T/H_C ratios of the negative samples increased continuously accompanied by the increased dilution ratio from 1/5 to 1/40, which was mainly caused by the reduced influence of the serum matrix (Fig. 7A). Meanwhile, due to the reduction of NAb concentration upon dilution, the H_T/H_C ratios of the positive samples gradually increased (Fig. 7A), which was solid evidence that the $AIE_{490}NP$-based LFIA was promising for quantitative detection of NAbs. As shown in Fig. 7B, the inhibition rates of both negative and positive samples continued to decrease with the increased dilution ratio. Comprehensively, the signal-to-noise ratio reached the highest when the dilution rate was 1/20 (Fig. 7C).

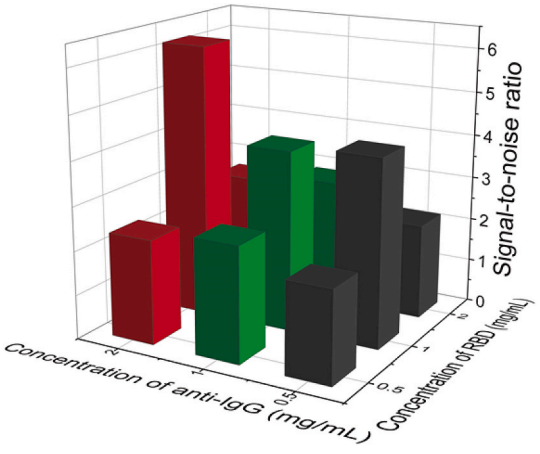

Fig. 5. The signal-to-noise ratio of the $AIE_{490}NP$-based LFIA under different concentrations of RBD coated on test line and anti-IgG coated on control line.

3.6. Practical detection of anti-SARS-CoV-2 NAb in clinical serum samples

To determine the detection threshold of the $AIE_{490}NP$-based LFIA for detecting anti-SARS-CoV-2 NAb in serum samples, 70 negative serum samples and 10 sample buffers were measured using this LFIA method to obtain the ratio of H_T/H_C (Fig. 8A and Table S4). The mean values of H_T/H_C for the negative serum samples and sample buffers had no significant difference. 63 positive serum samples from vaccinees were measured to obtain the H_T/H_C ratios (Fig. 8A and Table S5), which were apparently decreased compared to the negative serum samples and sample buffers. All the positive serum samples were collected from vaccinees with twice vaccination of inactivated vaccine from China one month after the second vaccination. The inhibition rates of these samples were calculated with the assistance of the average of 10 repeated measurements of the sample buffer (Fig. 8B). According to the average plus 3-fold standard deviation of inhibition rates of the negative samples, the detection threshold of anti-SARS-CoV-2 NAb was calculated to be 28.35. The obvious difference between the inhibition rates of negative samples and positive samples indicated that the $AIE_{490}NP$-based LFIA method could effectively distinguish whether a serum sample contains anti-SARS-CoV-2 NAb ($p < 0.0001$). The reproducibility was evaluated through testing five positive serum samples and five negative serum samples to determine the coefficient of variations (CVs) of intra- and inter-assay. As shown in Table 1, the intra- and inter-assay of negative samples were around 9.37–12.99% and 12.69–15.03%, respectively, while those of the positive samples were 6.81–7.58% and 7.15–8.44%, respectively. All the CVs were below or around 15%, indicating an acceptable reproducibility of the established $AIE_{490}NP$-based LFIA.

4. Discussion

We have proposed a well-applicable method that combined the AIE-PS nanoparticles and LFIA to achieve rapid and reliable detection of anti-SARS-CoV-2 NAb in human serums. The ultrabright AIE-PS nanoparticles were used as the marker to increase the sensitivity and shorten the detection time. The ultrabright nanoparticles-based LFIA has tremendous practical value of generalization as a rapid semi-quantitative detection method of anti-SARS-CoV-2 NAb.

The anti-SARS-CoV-2 NAb level in the body is becoming an indispensable reference to evaluate the acquired protective immunity for SARS-CoV-2 [28]. Among all the NAb detection methods, LFIA has unique advantages, such as low cost, easy operation, and no need for complex pretreatment and sophisticated instruments [9]. The marker for signal output is the key component that concerns the performance of LFIA. Until now, the colloidal gold nanoparticle is still the most common marker for LFIA, but it is mostly used in qualitative LFIA [29]. Fluorescent markers such as lanthanide chelate nanoparticles, QPs and organic dyes can enable LFIAs with quantitative detection capability. However, the lanthanide chelate nanoparticles are confined to the fixed fluorescence wavelength; the QPs exhibited a lack of fluorescence intensities; the traditional organic dyes were limited with the quenched fluorescence in the aggregate state, poor photochemical stability, and narrow Stokes shift [30]. In the detection process by using LFIA, the markers are usually gathered in the test line or control line to give the output signals [31]. In our designs, we used an AIEgen as the fluorescent marker to improve the performance of LFIA. The AIE_{490} we synthesized exhibited typical AIE property. Its fluorescence was extremely enhanced

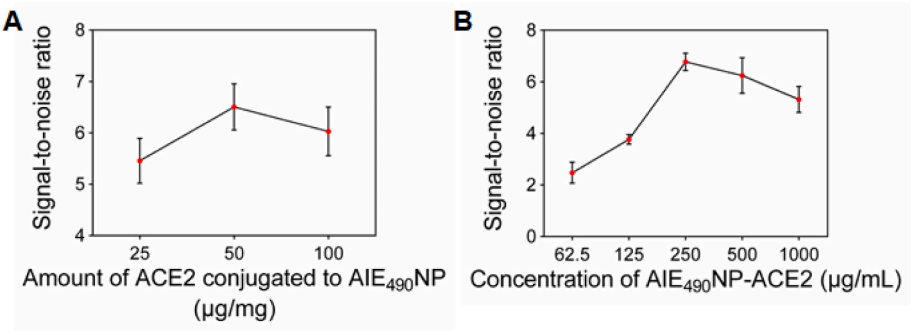

Fig. 6. (A) The signal-to-noise ratio of the AIE_{490}NP-based LFIA under different amount of ACE2 modified on the surface of AIE_{490}NP. (B) The signal-to-noise ratio of the AIE_{490}NP-based LFIA under different concentration of AIE_{490}NP-ACE2 used in the LFIA.

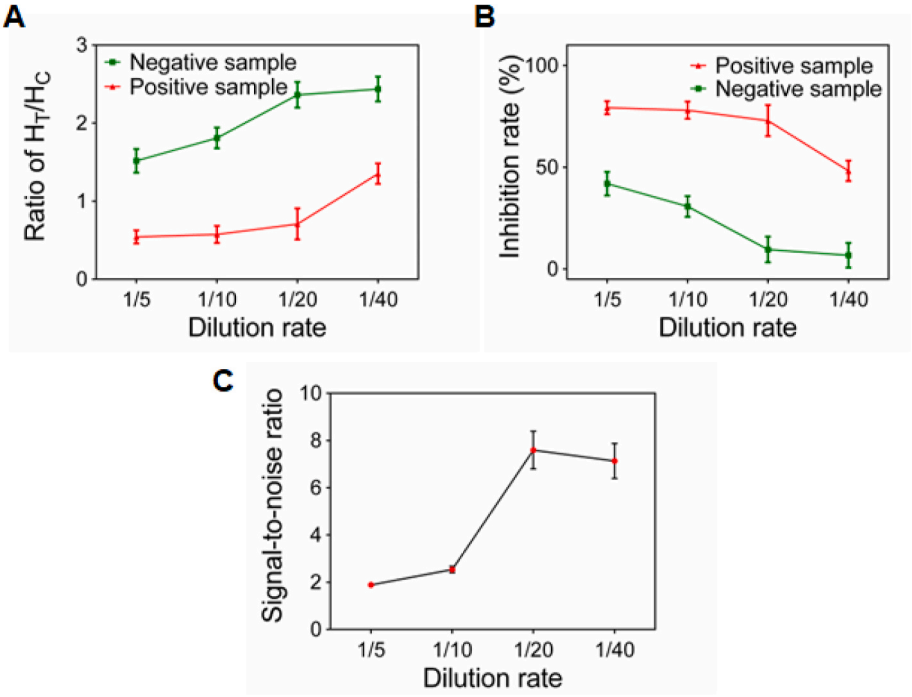

Fig. 7. The (A) H_T/H_C ratios and (B) inhibition rates of negative samples and positive samples under different dilution rates of serum samples. The average and standard deviation were calculated through five replications. (C) The signal-to-noise ratio of the AIE_{490}NP-based LFIA under different dilution rates of serum samples.

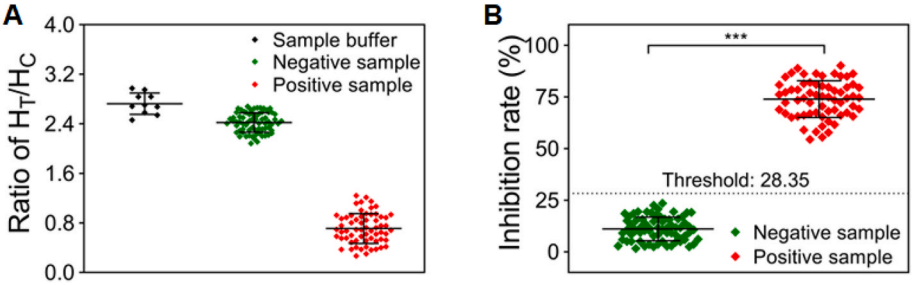

Fig. 8. (A) The H_T/H_C ratios of 10 sample buffer, 70 negative samples, and 63 positive samples. (B) The inhibition rates of 70 negative samples and 63 positive samples. The dashed line represents the threshold calculated as the average plus 3-fold standard deviation of inhibition rates of the negative samples to be 28.35. ***, $p < 0.001$.

when it turned to aggregate state in water. In this regard, AIE_{490} could overcome the quenched fluorescence of traditional organic dyes in aggregate state and satisfy the demand of LIFA better. Meanwhile, the excitation and emission wavelength of AIEgens are tunable. By designing the structure of AIEgen to change its emission wavelength, AIE nanoparticles can be better adapted to various LFIA detection instruments. The best excitation wavelength of AIE_{490} was 365 nm, which was a customized wavelength that matched the excitation light source of most portable detection instruments. As some AIEgens could be excited with the same laser but emit different colors of light, we will further try

Table 1
The reproducibility of the developed AIE_{490}NP-based LFIA.

		Intra-assay (n = 5)		Inter-assay (n = 10)	
		Inhibition rate (%)	CV (%)	Inhibition rate (%)	CV (%)
Negative samples	1	9.02 ± 0.85	9.37	9.38 ± 1.28	13.62
	2	14.00 ± 1.62	11.58	13.94 ± 2.09	15.03
	3	16.57 ± 1.75	10.62	16.43 ± 2.08	12.69
	4	12.35 ± 1.60	12.99	12.63 ± 1.82	14.44
	5	12.72 ± 1.61	12.69	12.90 ± 1.72	13.33
Positive samples	1	66.97 ± 4.56	6.81	67.44 ± 5.08	7.53
	2	70.22 ± 5.32	7.58	72.15 ± 5.80	8.04
	3	75.35 ± 5.56	7.37	75.97 ± 6.35	8.36
	4	65.88 ± 4.97	7.54	63.94 ± 4.57	7.15
	5	82.05 ± 5.62	6.85	79.99 ± 6.75	8.44

the multicolor markers-based LFIA to increase the detection sensitivity. The Stokes shift of AIE_{490} was 135 nm, which was large enough to distinguish the emission fluorescence from the excitation light. Therefore, the signal collector could easily and accurately read the outputs. All these advantages make AIE nanoparticles have broad prospects of application in LFIA even many other immunofluorescence sensors.

Though most hydrophobic AIEgens have a strong fluorescence in water, the aggregate format of an AIEgen does matter much about the fluorescence intensity. For example, the surfactant matrix-AIEgen nanoparticles are generally brighter than AIEgen precipitate in water [24]. The AIEgen crystals have much denser packing and exhibit ultrabright emission [25]. However, we found that neither the bright surfactant matrix-AIEgen nanoparticles nor the ultrabright AIEgen crystals could be used in LFIA due to the terrible release from the pad. In this work, we encapsulated AIE_{490} into the PS nanoparticles and found that the obtained AIE_{490}NP had an ultrabright fluorescence. The fluorescence intensity of AIE_{490}NP was twice that of the surfactant matrix-AIE_{490} nanoparticles, tenfold that of the precipitate of AIE_{490} in water. Furthermore, the fluorescence intensity of AIE_{490}NP was also much stronger than QPs (Fig. S10). We proposed that the ultrabright emission of AIE_{490}NP came from the rigidity of PS and severe inhibition of intramolecular motions of AIE_{490} in AIE_{490}NP. On the benefit of the ultrabright emission of AIE_{490}NP, the LFIA we designed could figure out the 70 negative serum samples and 63 positive serum samples without mistakes. Meanwhile, in the optimized conditions, the intra- (6.81–12.99%) and inter-assay (7.15–15.03%) of the AIE_{490}NP-based LFIA indicated an acceptable reproducibility. The performance of the AIE_{490}NP-based LFIA suggested much practical utility for the rapid detection of NAb levels in vaccinated sera.

The present AIE_{490}NP-based LFIA was designed to be a quantitative detection of anti-SARS-CoV-2 NAb in human serum, but it just achieved semi-quantitative function due to the lack of a golden standard for anti-SARS-CoV-2 NAb calibration. Until now, the specific level of anti-SARS-CoV-2 NAb that can effectively prevent or alleviate symptoms has not been reported. But there is no doubt that the higher levels of NAbs mean greater protection. Therefore, the current semi-quantitative detection mode through the detection of fluorescence signal intensity can meet the evaluation needs of NAbs in the stage of see. Once standards were available, present AIE_{490}NP-based LFIA could perform better.

5. Conclusions

In conclusion, an AIE_{490}NP-based LFIA was successfully established for rapid semi-quantitative detection of anti-SARS-CoV-2 NAb, which could achieve the detection within 20 min with one step. To verify the performance of the present AIE_{490}NP-based LFIA, 70 negative serum samples and 63 positive serum samples were measured. This present method could effectively distinguish the positive and negative serum samples. The intra- (6.81–12.99%) and inter-assay (7.15–15.03%) of the established AIE_{490}NP-based LFIA indicate an acceptable reproducibility. The performance of the established AIE_{490}NP-based LFIA suggests its potential as an alternative method for rapid detection of neutralizing antibody levels in vaccinated sera. At the same time, it also provides a basis investigation of multi-label AIE_{490}NP-based LFIA. And the AIE_{490}NP-based LFIA has great potential for various analytes detections, which deserve further research.

Credit author statement

Lun Bian: Methodology, Validation, Software, Writing – original draft, review, and editing. Zhaoyue Li: Investigation, manuscript revision. An He: Software, Data curation. Biru Wu: Investigation, Methodology, Software, synthesis and characterization of materials. Hui Yang: exploration of conditions for nanoparticles synthesis. Yingsong Wu: Conceptualization, Methodology. Fang Hu: Conceptualization, Methodology, Funding acquisition, writing, review, and editing. Guanfeng Lin: Conceptualization, Methodology, Funding acquisition, writing, review, and editing. Deqing Zhang: discussion and review.

Declaration of competing interest

The authors declare that they have no known competing financial interests or personal relationships that could have appeared to influence the work reported in this paper.

Data availability

Data will be made available on request.

Acknowledgments

We are grateful for the financial support of the National Natural Science Foundation of China (22077060), Guangdong Basic and Applied Basic Research Foundation (2019A1515110241).

Appendix A. Supplementary data

Supplementary data to this article can be found online at https://doi.org/10.1016/j.biomaterials.2022.121694.

References

[1] M.B. Oude, N. Worp, D.F. Nieuwenhuijse, R.S. Sikkema, B. Haagmans, R. Fouchier, M. Koopmans, The next phase of SARS-CoV-2 surveillance: real-time molecular epidemiology, Nat. Med. 27 (2021) 1518–1524.
[2] K.E. Stephenson, M. Le Gars, J. Sadoff, A.M. de Groot, D. Heerwegh, C. Truyers, C. Atyeo, C. Loos, A. Chandrashekar, K. McMahan, L.H. Tostanoski, J. Yu, M. S. Gebre, C. Jacob-Dolan, Z. Li, S. Patel, L. Peter, J. Liu, E.N. Borducchi, J. P. Nkolola, M. Souza, C.S. Tan, R. Zash, B. Julg, R.R. Nathavitharana, R.L. Shapiro, A.A. Azim, C.D. Alonso, K. Jaegle, J.L. Ansel, D.G. Kanjilal, C.J. Guiney, C. Bradshaw, A. Tyler, T. Makoni, K.E. Yanosick, M.S. Seaman, D.A. Lauffenburger, G. Alter, F. Struyf, M. Douoguih, J. Van Hoof, H. Schuitemaker, D.H. Barouch, Immunogenicity of the Ad26.COV2.S vaccine for COVID-19, JAMA 325 (2021) 1535–1544.
[3] R. Chen, C. Ren, M. Liu, X. Ge, M. Qu, X. Zhou, M. Liang, Y. Liu, F. Li, Early detection of SARS-CoV-2 seroconversion in humans with aggregation-induced near-infrared emission nanoparticle-labeled lateral flow immunoassay, ACS Nano 15 (2021) 8996–9004.
[4] S.J. Zost, P. Gilchuk, J.B. Case, E. Binshtein, R.E. Chen, J.P. Nkolola, A. Schäfer, J. X. Reidy, A. Trivette, R.S. Nargi, R.E. Sutton, N. Suryadevara, D.R. Martinez, L. E. Williamson, E.C. Chen, T. Jones, S. Day, L. Myers, A.O. Hassan, N.M. Kafai, E. S. Winkler, J.M. Fox, S. Shrihari, B.K. Mueller, J. Meiler, A. Chandrashekar, N. B. Mercado, J.J. Steinhardt, K. Ren, Y.M. Loo, N.L. Kallewaard, B.T. McCune, S. P. Keeler, M.J. Holtzman, D.H. Barouch, L.E. Gralinski, R.S. Baric, L.B. Thackray, M.S. Diamond, R.H. Carnahan, J.J. Crowe, Potently neutralizing and protective human antibodies against SARS-CoV-2, Nature 584 (2020) 443–449.
[5] D. Wrapp, N. Wang, K.S. Corbett, J.A. Goldsmith, C.L. Hsieh, O. Abiona, B. S. Graham, J.S. McLellan, Cryo-EM structure of the 2019-nCoV spike in the prefusion conformation, Science 367 (2020) 1260–1263.
[6] L. Horndler, P. Delgado, D. Abia, I. Balabanov, P. Martinez-Fleta, G. Cornish, M. A. Llamas, S. Serrano-Villar, F. Sanchez-Madrid, M. Fresno, H.M. van Santen, B. Alarcon, Flow cytometry multiplexed method for the detection of neutralizing

human antibodies to the native SARS-CoV-2 spike protein, EMBO Mol. Med. 13 (2021), e13549.
[7] C.P. Thompson, N.E. Grayson, R.S. Paton, J.S. Bolton, J. Lourenco, B.S. Penman, L. N. Lee, V. Odon, J. Mongkolsapaya, S. Chinnakannan, W. Dejnirattisai, M. Edmans, A. Fyfe, C. Imlach, K. Kooblall, N. Lim, C. Liu, C. Lopez-Camacho, C. McInally, A. L. McNaughton, N. Ramamurthy, J. Ratcliff, P. Supasa, O. Sampson, B. Wang, A. J. Mentzer, M. Turner, M.G. Semple, K. Baillie, H. Harvala, G.R. Screaton, N. Temperton, P. Klenerman, L.M. Jarvis, S. Gupta, P. Simmonds, Detection of neutralising antibodies to SARS-CoV-2 to determine population exposure in Scottish blood donors between March and May 2020, Euro Surveill. 25 (2020).
[8] X.C. Le, Analytical advances in detecting SARS-CoV-2 and further research needs for COVID-19 testing, Anal. Chem. 93 (2021) 8379–8380.
[9] X. Duan, Y. Shi, X. Zhang, X. Ge, R. Fan, J. Guo, Y. Li, G. Li, Y. Ding, R.A. Osman, W. Jiang, J. Sun, X. Luan, G. Zhang, Dual-detection fluorescent immunochromatographic assay for quantitative detection of SARS-CoV-2 spike RBD-ACE2 blocking neutralizing antibody, Biosens. Bioelectron. 199 (2022), 113883.
[10] S.C. Taylor, B. Hurst, C.L. Charlton, A. Bailey, J.N. Kanji, M.K. McCarthy, T. E. Morrison, L. Huey, K. Annen, M.G. DomBourian, V. Knight, A new SARS-CoV-2 dual-purpose serology test: highly accurate infection tracing and neutralizing antibody response detection, J. Clin. Microbiol. 59 (2021).
[11] S.N. Walker, N. Chokkalingam, E.L. Reuschel, M. Purwar, Z. Xu, E.N. Gary, K. Y. Kim, M. Helble, K. Schultheis, J. Walters, S. Ramos, K. Muthumani, T. Smith, K. E. Broderick, P. Tebas, A. Patel, D.B. Weiner, D.W. Kulp, SARS-CoV-2 assays to detect functional antibody responses that block ACE2 recognition in vaccinated animals and infected patients, J. Clin. Microbiol. 58 (2020).
[12] S.S. Mahshid, S.E. Flynn, S. Mahshid, The potential application of electrochemical biosensors in the COVID-19 pandemic: a perspective on the rapid diagnostics of SARS-CoV-2, Biosens. Bioelectron. 176 (2021), 112905.
[13] M. Torres, W.R. de Araujo, L.F. de Lima, A.L. Ferreira, C. de la Fuente-Nunez, Low-cost biosensor for rapid detection of SARS-CoV-2 at the point of care, Matter 4 (2021) 2403–2416.
[14] C.W. Tan, W.N. Chia, X. Qin, P. Liu, M.I. Chen, C. Tiu, Z. Hu, V.C. Chen, B. E. Young, W.R. Sia, Y.J. Tan, R. Foo, Y. Yi, D.C. Lye, D.E. Anderson, L.F. Wang, A SARS-CoV-2 surrogate virus neutralization test based on antibody-mediated blockage of ACE2-spike protein-protein interaction, Nat. Biotechnol. 38 (2020) 1073–1078.
[15] B.K. Sil, M.R. Jamiruddin, M.A. Haq, M.U. Khondoker, N. Jahan, S.S. Khandker, T. Ali, M.J. Oishee, T. Kaitsuka, M. Mie, K. Tomizawa, E. Kobatake, M. Haque, N. Adnan, AuNP coupled rapid flow-through dot-blot immuno-assay for enhanced detection of SARS-CoV-2 specific nucleocapsid and receptor binding domain IgG, Int. J. Nanomed. 16 (2021) 4739–4753.
[16] H.Y. Kim, J.H. Lee, M.J. Kim, S.C. Park, M. Choi, W. Lee, K.B. Ku, B.T. Kim, P. E. Changkyun, H.G. Kim, S.I. Kim, Development of a SARS-CoV-2-specific biosensor for antigen detection using scFv-Fc fusion proteins, Biosens. Bioelectron. 175 (2021), 112868.
[17] D. Quesada-Gonzalez, A. Merkoci, Nanoparticle-based lateral flow biosensors, Biosens. Bioelectron. 73 (2015) 47–63.
[18] J. Jia, L. Ao, Y. Luo, T. Liao, L. Huang, D. Zhuo, C. Jiang, J. Wang, J. Hu, Quantum dots assembly enhanced and dual-antigen sandwich structured lateral flow immunoassay of SARS-CoV-2 antibody with simultaneously high sensitivity and specificity, Biosens. Bioelectron. 198 (2022), 113810.
[19] K.W. Lee, K.R. Kim, H.J. Chun, K.Y. Jeong, D.K. Hong, K.N. Lee, H.C. Yoon, Time-resolved fluorescence resonance energy transfer-based lateral flow immunoassay using a raspberry-type europium particle and a single membrane for the detection of cardiac troponin I, Biosens. Bioelectron. 163 (2020), 112284.
[20] S.W. Dai, Y.L. Lai, L. Yang, Y.T. Chuang, G.H. Tan, S.W. Shen, Y.S. Huang, Y.C. Lo, T.H. Yeh, C.I. Wu, L.J. Chen, M.Y. Lu, K.T. Wong, S.W. Liu, H.W. Lin, Organic lead halide nanocrystals providing an ultra-wide color gamut with almost-unity photoluminescence quantum yield, ACS Appl. Mater. Interfaces 13 (2021) 25202–25213.
[21] X. Hu, P. Zhang, D. Wang, J. Jiang, X. Chen, Y. Liu, Z. Zhang, B.Z. Tang, P. Li, AIEgens enabled ultrasensitive point-of-care test for multiple targets of food safety: aflatoxin B1 and cyclopiazonic acid as an example, Biosens. Bioelectron. 182 (2021), 113188.
[22] H. Zhang, Z. Zhao, A.T. Turley, L. Wang, P.R. McGonigal, Y. Tu, Y. Li, Z. Wang, R. Kwok, J. Lam, B.Z. Tang, Aggregate science: from structures to properties, Adv. Mater. 32 (2020), e2001457.
[23] J. Mei, N.L. Leung, R.T. Kwok, J.W. Lam, B.Z. Tang, Aggregation-induced emission: together we shine, united we soar, Chem. Rev. 115 (2015) 11718–11940.
[24] G. Feng, B. Liu, Aggregation-induced emission (AIE) dots: emerging theranostic nanolights, Acc. Chem. Res. 51 (2018) 1404–1414.
[25] S.M. Fateminia, Z. Wang, C.C. Goh, P.N. Manghnani, W. Wu, D. Mao, L.G. Ng, Z. Zhao, B.Z. Tang, B. Liu, Nanocrystallization: a unique approach to yield bright organic nanocrystals for biological applications, Adv. Mater. 29 (2017).
[26] Z. Chen, P. Li, Z. Zhang, X. Zhai, J. Liang, Q. Chen, K. Li, G. Lin, T. Liu, Y. Wu, Ultrasensitive sensor using quantum dots-doped polystyrene nanospheres for clinical diagnostics of low-volume serum samples, Anal. Chem. 91 (2019) 5777–5785.
[27] Z. Chen, R. Liang, X. Guo, J. Liang, Q. Deng, M. Li, T. An, T. Liu, Y. Wu, Simultaneous quantitation of cytokeratin-19 fragment and carcinoembryonic antigen in human serum via quantum dot-doped nanoparticles, Biosens. Bioelectron. 91 (2017) 60–65.
[28] G. Lippi, B.M. Henry, M. Plebani, Anti-SARS-CoV-2 antibodies testing in recipients of COVID-19 vaccination: why, when, and how? Diagnostics 11 (2021) 941.
[29] F. Di Nardo, M. Chiarello, S. Cavalera, C. Baggiani, L. Anfossi, Ten years of lateral flow immunoassay technique applications: trends, challenges and future perspectives, Sensors 21 (2021) 5185.
[30] X. Gong, J. Cai, B. Zhang, Q. Zhao, J. Piao, W. Peng, W. Gao, D. Zhou, M. Zhao, J. Chang, A review of fluorescent signal-based lateral flow immunochromatographic strips, J. Mater. Chem. B 5 (2017) 5079–5091.
[31] K.M. Koczula, A. Gallotta, Lateral flow assays, Essays Biochem. 60 (2016) 111–120.